Volumetric Intraoperative Brain Deformation Compensation: Model Development and Phantom Validation

Christine DeLorenzo*, Xenophon Papademetris, Lawrence H. Staib, Kenneth P. Vives, Dennis D. Spencer, and James S. Duncan

Abstract—During neurosurgery, nonrigid brain deformation may affect the reliability of tissue localization based on preoperative images. To provide accurate surgical guidance in these cases, preoperative images must be updated to reflect the intraoperative brain. This can be accomplished by warping these preoperative images using a biomechanical model. Due to the possible complexity of this deformation, intraoperative information is often required to guide the model solution. In this paper, a linear elastic model of the brain is developed to infer volumetric brain deformation associated with measured intraoperative cortical surface displacement. The developed model relies on known material properties of brain tissue, and does not require further knowledge about intraoperative conditions. To provide an initial estimation of volumetric model accuracy, as well as determine the model's sensitivity to the specified material parameters and surface displacements, a realistic brain phantom was developed. Phantom results indicate that the linear elastic model significantly reduced localization error due to brain shift, from > 16 mm to under 5 mm, on average. In addition, though *in vivo* quantitative validation is necessary, preliminary application of this approach to images acquired during neocortical epilepsy cases confirms the feasibility of applying the developed model to *in vivo* data.

Index Terms—Brain modeling, image processing, image registration, image-guided neurosurgery.

I. INTRODUCTION

SURGICAL navigation systems (SNS) can provide real-time visualization of surgical tool positions relative to a patient's preoperative brain images. These systems provide neurosurgeons with visual verification of pathologic tissue located beneath exposed brain tissue. As long as the preoperative images accurately reflect the intraoperative brain, neurosurgeons can rely on SNS for guidance. However, during

*C. DeLorenzo is with the Department of Psychiatry, Columbia University, New York, NY 10032 USA.

X. Papademetris, L. H. Staib, and J. S. Duncan are with the Department of Biomedical Engineering, Yale University, New Haven, CT 06520 USA (e-mail: christine.delorenzo@aya.yale.edu).

K. P. Vives and D. D. Spencer are with the Department of Neurosurgery, Yale–New Haven Hospital, New Haven, CT 06520 USA.

surgery, gravity, loss of blood and cerebrospinal fluid (CSF), or the action of certain medications may cause soft tissue deformation. This deformation, referred to as brain shift, can cause significant misalignment between preoperative brain images and the intraoperative brain ([2], [18], [39], [40]). Accounting for this brain shift is therefore necessary to realize the effectiveness of SNS and to allow surgeons to confidently excise tissue, especially near functionally eloquent areas.

Because multiple factors can affect the type and extent of brain shift, it may not be possible to predict the magnitude of the deformation before surgery. For this reason, most techniques aimed at improving neurosurgical navigation are limited to compensating for the shift after it has occurred. These brain shift compensation methods can be broadly divided into two categories. The first category involves acquiring full volumetric images during surgery, and the second involves acquiring sparse intraoperative information and using this data in conjunction with a biomechanical brain model.

The first category of brain shift compensation requires modalities such as intraoperative computed tomography (iCT), magnetic resonance imaging (iMRI), or ultrasound (iUS) ([4], [5], [18], [19], [21], [28], [32], [39], [52]). While these techniques can provide visualization of the entire brain during surgery, their disadvantages include radiation exposure (iCT), poor imaging contrast (iUS), necessity of intermodality registration (iUS/iCT), cost (iMRI), and the need to suspend surgery to acquire images (iUS/iCT/iMRI).

Sparse information for the second class of methods can be acquired by imaging the exposed cortical surface using stereo cameras or laser range scanners ([2], [11], [12], [25], [36], [42], [43], [45], [47]). These techniques only acquire information at the surface and therefore must rely on biomechanical models for volumetric deformation estimates. However, the intraoperative acquisitions are often markedly shorter and have the potential to be performed without disrupting surgery. Also, due to their quick acquisition times, this second class of methods can be used in conjunction with full volumetric imaging. For example, when surface-based deformation estimates reach a certain threshold, a full volumetric image can be acquired. In this way, deformation estimates would be available between volumetric acquisitions, and help inform decisions about the need for these longer acquisitions.

Due to its time and cost advantages, surface imaging and a brain biomechanical model were used to track intraoperative brain shift in this work. To this end, a biomechanical model was developed for determination of volumetric brain deformation.

This model only requires the cortical displacement (as found with any cortical surface tracking technique) and the material properties of brain as inputs. It has been developed such that effects of any external (e.g., gravity) or internal (e.g., loss of CSF) forces are relayed through the surface deformation and do not need to be explicitly estimated. Difficult estimations of patient head orientation (to determine gravity effects) or the amount of blood or CSF loss, as required by other, more complex models ([12], [43]) are therefore unnecessary. In addition, there is no constraint on the timing of the intraoperative acquisitions, unlike similar models that require data acquisition immediately after dura opening in order to perform a closest point matching between the initial brain surface (assumed to have little or no deformation) and the preoperative brain ([10]–[13], [42], [44], [47]). This is a great advantage since significant brain shift can occur with the opening of the dura [18], and acquisition time constraints may be difficult to meet in a busy operating room (OR).

In order to validate the model-predicted volumetric deformation estimates, a novel, realistic phantom, including both brain and the surrounding skull, was developed. Use of such a phantom can be extremely valuable for development, testing, and initial validation of biomechanical models, and allows measurement of volumetric deformation in a controlled environment. Since the most important aspect of this phantom is its mechanical behavior, it was constructed using a silicone gel with linear elastic properties matching the brain. The silicone gel was cured inside a skull mold, constructed based on an actual neurosurgical patient's magnetic resonance imaging (MRI). This phantom is easy to use, can be subjected to measured deformations (for repeatable testing conditions), and is reusable.

Using this realistic phantom, analysis was performed to investigate the sensitivity of the developed linear elastic model to both material parameter choice and the initial conditions imposed by the surface displacement estimation. The results of this analysis shed light on the effect of these parameters on the model solution. Following the phantom analysis, the developed biomechanical model was applied to four neocortical epilepsy surgical cases to determine the feasibility of applying this technique to *in vivo* data.

II. METHOD

The method for intraoperative brain shift compensation can be divided into two main steps (see Fig. 1). 1) Surface Deformation Estimation: The displacement of the exposed cortical surface is determined in this step. A game theoretic algorithm has previously been developed by our group for this calculation [14]; however, any method for determining cortical surface displacement can be used, including laser range scanning or direct estimation from stereo images ([2], [11], [25], [36], [42], [43], [47]). 2) Volumetric Determination: At this stage, the surface deformation estimation is extended through the brain volume using a biomechanical model. The development of this step is the main contribution of this work.

A. Intraoperative Deformation Estimation

In this work, a stereo imaging system was used to track the deforming cortical surface, as described in DeLorenzo *et al.* [14]. Since these stereo systems are often plagued with calibration
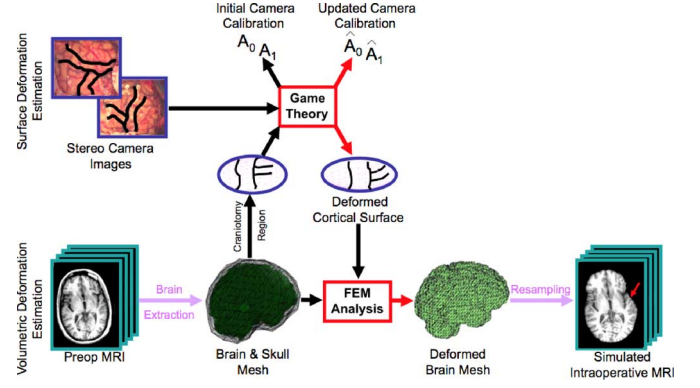

Fig. 1. Brain shift compensation flow chart. The first step (top row) consists of estimating the surface deformation. In this work, a game theoretic algorithm is used for this estimation (see Section II-A). The second step (bottom row) consists of the volumetric deformation estimation (see Section II-B). To accomplish this, the brain and skull are first extracted from the preoperative MRI. These volumes serve as inputs, along with the deformed cortical surface (output of the surface deformation estimation), to the volume calculation. The result of the volumetric calculation is the deformed position of every brain mesh node. This mesh is then resampled into the original image space to yield a simulated intraoperative MRI. The red arrow in this image indicates the region of greatest deformation. This intraoperative MRI can then be used to revise the preoperative surgical path.

error, image-derived estimates of deformation can be difficult. Because of this, game theory was used to disentangle the measured surface displacement from the effects of an inaccurate camera calibration. The inputs to the game theoretic algorithm are 1) an initial stereo camera calibration and 2) the preoperative cortical surface, as extracted from the preoperative MRI. The game theoretic formulation is then used to iteratively estimate the cortical surface deformation from the brain's preoperative position, by displacing the preoperative surface until projections of sulci on the deforming surface match their corresponding locations in the intraoperative stereo images, while incorporating surface intensity and smoothness information. The predicted deformed sulci and their corresponding image locations are then used, along with locations of sparse fiducial markers (used to calculate the initial camera calibration parameters), to update the camera calibration estimates at each iteration. The result of this algorithm is the 3-D displacement field of the exposed cortical surface and a refined camera calibration.

The final model is divided into two objective functions, one that is used to update the cortical displacement field estimation $(\mathcal{C}_1)$ and one that is used to update the camera calibration parameters $(\mathcal{C}_2)$

$$\mathcal{C}_1(\underline{\mathbf{U}}_{\text{dense}}, \underline{\mathbf{A}}) = \underbrace{T_U(\underline{\mathbf{U}}_{\text{dense}})}_{\text{smoothness constraint}}$$

$$+ \alpha \left[\underbrace{T_F(\underline{\mathbf{U}}_{\text{dense}}, \underline{\mathbf{A}})}_{\text{feature matching}} + \underbrace{T_I(\underline{\mathbf{U}}_{\text{dense}}, \underline{\mathbf{A}})}_{\text{intensity correlation}} \right]$$

$$\mathcal{C}_2(\underline{\mathbf{U}}_{\text{dense}}, \underline{\mathbf{A}}) = \underbrace{T_A(\underline{\mathbf{A}})}_{\text{fiducial matching}}$$

$$+ \beta \left[\underbrace{T_C(\underline{\mathbf{U}}_{\text{dense}}, \underline{\mathbf{A}})}_{\text{reconstructed sulci matching}} \right] \quad (1)$$

where α and β are constants, determined from the rules governing game theory [14], $\underline{\mathbf{U}}_{\text{dense}}$ is the dense displacement field applied to the cortical surface in the region of the craniotomy, and $\underline{\mathbf{A}} = [\underline{A_0}, \underline{A_1}]$, the camera calibration parameters (rotation, translation, focal length, principal point, lens distortion and skew coefficient) for the two camera positions (0 and 1). These objective functions are iteratively minimized ($\mathcal{C}_1$ with respect to $\underline{\mathbf{U}}_{\text{dense}}$ and $\mathcal{C}_2$ with respect to $\underline{\mathbf{A}}$) using gradient descent optimization. The algorithm functions are briefly defined below.

1) Displacement Field Determination: Three terms define the displacement field objective function. The first is a prior term, T_U, which ensures that the surface deformation is smooth. $T_U(\underline{\mathbf{U}}_{\text{dense}}) = \rho e^{-\int |U''_{\text{dense}}| dS}$, where U''_{dense} is the second derivative of the dense displacement field, $\overline{S}$ is the deformed surface over which the integral is taken, and ρ is a normalizing constant. This, and subsequent normalization constants, ensure that all terms have similar orders of magnitude.

A feature term, T_F, determines the distance between the 3-D sulci from the exposed cortical surface, $\underline{\mathbf{C}}$, which are projected onto the stereo images using a standard camera projection function (P[49]), and the intraoperative sulci outlined in those images, $\underline{\mathbf{K}} = [\underline{K_0}, \underline{K_1}]$. (Sulci are currently manually outlined by an expert user, although automation can be added to this procedure [14].)

$$T_F(\underline{\mathbf{U}}_{\text{dense}}, \underline{\mathbf{A}}) = -\left(\int d[\underline{K_0}, P(A_0, (\underline{\mathbf{C}} + \underline{\mathbf{U}}^C_{\text{dense}}))]dS \right.$$
$$\left. + \int d[\underline{K_1}, P(A_1, (\underline{\mathbf{C}} + \underline{\mathbf{U}}^C_{\text{dense}}))]dS \right)$$

where $\underline{\mathbf{U}}^C_{\text{dense}}$ is the dense displacement field restricted to the sulci, d is a function that calculates the mean Euclidean distance between two curves.

The last term, T_I, matches the image intensities from each camera position, which are backprojected onto the exposed brain surface (see Fig. 6(C) and (D) for examples). Here, a backprojected image is defined as $B_i^S = I_i(P(A_i, x)) \forall x \in S$, where I_i is an intraoperative stereo image from camera position $i = 0,1$ [44]. $T_I(\underline{\mathbf{U}}_{\text{dense}}, \underline{\mathbf{A}}) = \eta \text{NCC}(B_0^S, B_1^S)$, where NCC is the normalized cross correlation [14] and η is a normalizing constant.

2) Camera Calibration Optimization: The initial camera calibration is performed by acquiring the 3-D locations of fiducial points on the cortical surface and their 2D stereo image locations, and then finding the best fit transformation between those two point sets [49]. Therefore, a prior on the camera calibration, T_A, ensures that, as the camera parameters are updated, the projection of the n fiducial points, $L_{0...n}$, onto the stereo images are close to imaged fiducial points from camera positions 0 and 1, $m_{0i...n}$ and $m_{1i...n}$, respectively. This can be expressed as $T_A(\underline{\mathbf{A}}) = \sum_{i=1}^{n} \|[P(A_0, Li) - m_{0i}]\| + \|[P(A_1, Li) - m_{1i}]\|$.

The second term in the camera calibration optimization, T_C, takes advantage of the cortical surface features. Using standard stereo camera geometry, a function, Φ, that reconstructs a point in 3-D space using the calibration parameters and the point's location in each stereo image, can be written [49]. With this function, the sulci from the images can be reconstructed in 3-D space and compared to their positions on the deformed cortical surface. (The distance between the preoperative sulci on the MRI surface and the stereo imaged sulci reconstructed using Φ provides the initialization for the dense displacement field.) The can be written as $T_C(\underline{\mathbf{U}}_{\text{dense}}, \underline{\mathbf{A}}) = \int d\left[\Phi(K_0, K_1, \underline{\mathbf{A}}), (\underline{\mathbf{C}} + \underline{\mathbf{U}}^C_{\text{dense}}) \right] dS$.

3) Comparison to Other Surface Tracking Methods: The game theoretic method described above shares many features with other deformation compensation techniques that rely on cortical surface features such as sulci or blood vessels. For example, some surface based algorithms warp preoperative image features to their intraoperative positions using robust point matching [10], an iterative closest point technique [48], or a deformable model [44]. As another example of these techniques, interesting work was performed by Ding *et al.*, in which cortical vessels were semiautomatically delineated using a minimum cost path algorithm, and then tracked in images pre and post tumor resection [15], or in subsequent video frames (with and without occlusion by surgical instruments) [16].

Similar to these feature-based methods, two of the terms in the game theoretic model rely on matching imaged sulci. Since vessels often parallel sulcal and gyral patterns, there are great similarities between these methods [31]. In addition, any method relying on surface imaging with visible light requires both a camera calibration [essentially a minimization of $T_A(\underline{\mathbf{A}})$ in (1)] and the use of a similarity metric for matching intensities [as in $T_I(\underline{\mathbf{U}}_{\text{dense}}, \underline{\mathbf{A}})$, (1)].

Although many surface-based techniques do share common features with the game theoretic algorithm, any method yielding the deformation of the cortical surface, regardless of how it is developed, can be used to generate the displacement initial conditions for the volumetric deformation algorithm described below. This provides the flexibility of tailoring the surface tracking choice to the surgery type, minimizing requirements for the exposed intraoperative surface. For example, stereo-camera-based deformation compensation can be applied in many neurosurgical procedures (since dural openings ≥ 4 cm in diameter will allow for adequate intensity/feature detection). In surgeries in which the craniotomies are smaller, or the surgical field is occluded by tools or equipment, it may be difficult or impossible to track the cortical surface using stereo cameras (or laser range sensors). However, in these surgeries, surface deformation estimates may still be acquired using techniques such as intraoperative ultrasound ([5], [19], [28]) or manually tracked anatomical surface locations [45]. These deformed surface estimates, or any sparse set of known displacements, can be used as inputs to the volumetric algorithm.

B. Volumetric Determination

Previous work has shown that linear elastic models (LEMs) can accurately estimate brain deformation during surgery ([1], [13], [29], [45], [46], [55]). For example, an LEM was chosen by Archip *et al.* since it was the only model that could meet the extreme time constraints of neurosurgical procedures, defined as ~ 20 min to final visualization [1]. Both Archip *et al.* [1] and Clatz *et al.* [13] utilized a biomechanical model driven by image intensities and tissue mechanical properties. In experiments by Paulsen *et al.* [37], Navier's equation was shown to
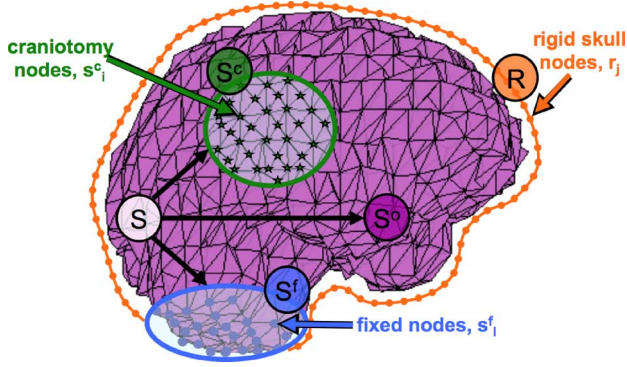
Fig. 2. Depiction of the various node types on the brain mesh surface. A profile of the skull constraint is shown for reference. The actual skull surface covers the whole brain mesh except for the fixed node and craniotomy regions. An explanation of each of these variables is in the text.

predict the displacement of brain tissue when subject to a body force. In interesting extensions of that work, the poroelastic model achieved accurate results when guided by surface data or fiducial marker displacement and solved inversely ([17], [29]). Škrinjar *et al.* also showed that volumetric results could be obtained by relying solely on direct measurements of the cortical surface as displacement boundary conditions for an LEM [45].

Nonlinear [53] or anisotropic [26] brain models have the potential to incrementally improve LEM deformation calculations in some areas of the brain; however, they require more computation, brain parameter estimation or additional imaging, such as diffusion tensor imaging (DTI). Additionally, the comparison between these and homogeneous linear models has been limited and generally based on small deformations. For these reasons, as well as ease of implementation, an LEM was developed in this work to extend cortical surface deformations to the brain volume.

The developed LEM was applied using finite element analysis throughout the brain volume, which was discretized into tetrahedral mesh elements. Mesh generation was performed with inhouse software, which uses geometric constraints to discretize a binary image (in which brain voxels were set to an intensity of one and nonbrain voxels, i.e., ventricles, CSF, dura, skull, and background, were set to zero). As part of the mesh generation, the software automatically labeled each node as belonging to the either the brain volume V or surface S. These surface nodes were further manually classified as belonging to the exposed craniotomy region S^c, fixed region S^f, or other (unconstrained nodes) S^o. The fixed surface region was defined at the base of the brain in the inferior occipital lobes. (Due to the tough tentorium cerebelli, as well as their distance from the craniotomy site, these nodes should not move during surgery.) A rigid mesh representing the skull (with craniotomy nodes removed) was also included at a fixed distance from the brain surface to realistically constrain the deformation (see Fig. 2).

In LEMs, the stress on a material σ is related to the material strain ϵ by $\sigma = C\epsilon$, where C is the material stiffness matrix. Using this relationship, deformation throughout the whole brain can be calculated by an energy minimization framework [34] in conjunction with constraints from known displacements and brain anatomy. This yields the strain energy density for-
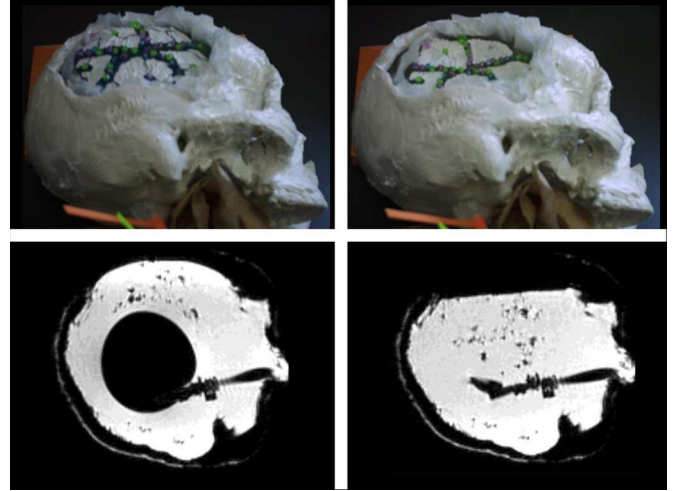

Fig. 3. Phantom surface movement (top) with corresponding MR images (bottom). The images in the left column show the inflated balloon embedded within the brain phantom. The images in the right column show the phantom with the inner balloon deflated. Once the air is removed, the surface sinks inward, mimicking intraoperative brain shift.
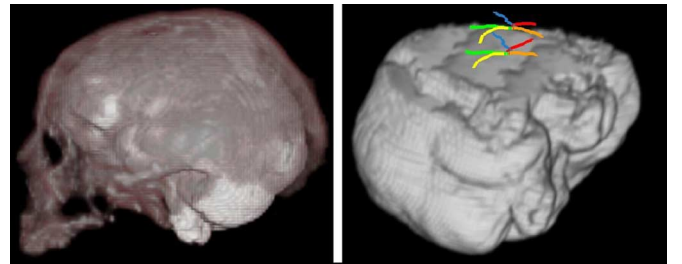

Fig. 4. Volume rendering of silicone brain and skull phantom from magnetic resonance images. The image on the left shows the brain phantom inside of the skull mold, which is colored for contrast. The right image shows the phantom brain volume with the skull stripped to reveal the shape formed by the gel against the mold. The multicolored lines show the positions of the beaded surface features with the inner balloon inflated (above the volume) and deflated (against the surface). This image was acquired with the inner balloon deflated.
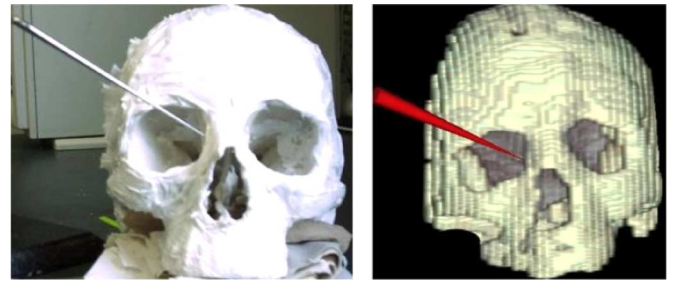

Fig. 5. The actual brain and skull phantom is shown on the left with the BrainLAB pointer aimed at the bridge of the nose. The registered volume rendered MRI of the phantom is shown on the right. Using BioImage Suite software [33], the location and orientation of the pointer can be displayed (red) and saved.

mulation, which relates the work done per unit volume to the deformation (v) [6]

$$\hat{v} = \arg\min_{v} \left(\int_B W(v, m, E, \nu) dB \right) \quad (2)$$

where B is the entire brain volume, consisting of all nodes $(B = V \bigcup S)$, and $W(v, m, E, \nu)$ is a positive semi-definite

(A) Deflated Stereo Images with Features Highlighted (Red) and Projected Inflated Features (Green)

(B) Deflated Stereo Images with Features Highlighted (Red) and Projected Predicted Features (Yellow)

(C) Inflated Surface Position & Features (Green) with Deflated Image Backprojections

(D) Predicted Surface Position & Features (Yellow) with Deflated Image Backprojections
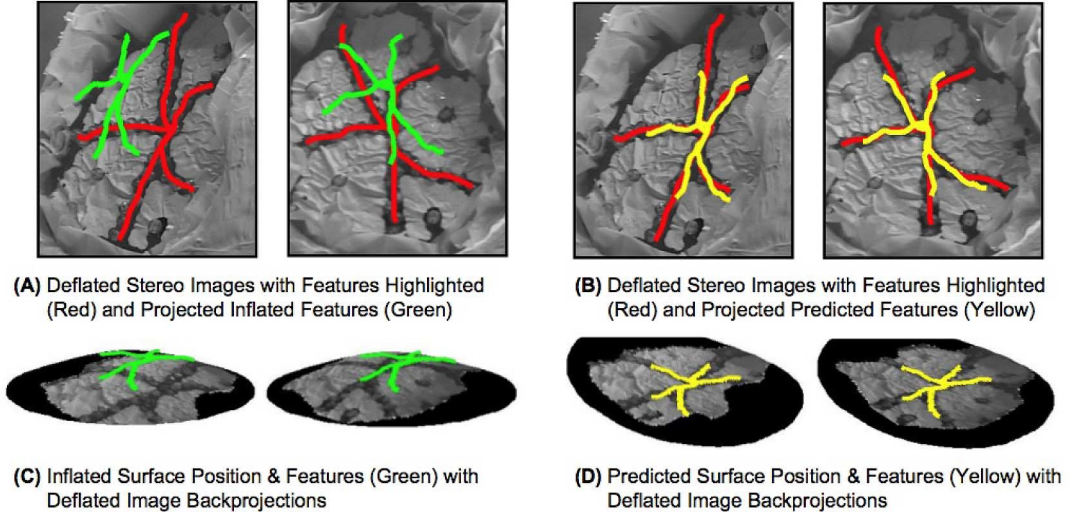
Fig. 6. Top: Stereo images of the deflated surface. (A) Features from the inflated surface projected onto the stereo images (green). These features are not aligned with the ones seen in the image (red) due to the deformation of the surface and possible calibration errors. (B) The features from the predicted surface projected onto the stereo images with updated calibration parameters (yellow). These projected features are closely aligned with their imaged positions (red). Bottom: Backprojections of the deflated phantom surface images. The shape of the original (inflated) phantom surface is shown in (C), while the predicted surface is shown in (D). The predicted surface not only aligns the intensities backprojected from the stereo images, but also matches the surface feature locations (as extracted from the MRI, yellow) with the backprojected image feature locations (imaged beads).
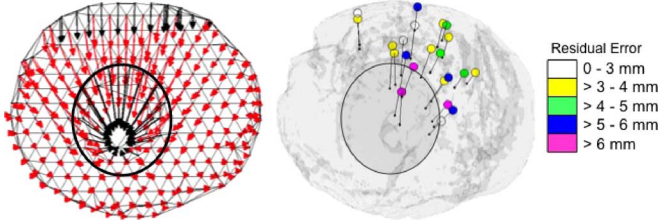

Fig. 7. The left side shows an axial slice of the volumetric phantom. Black arrows indicate the enforced displacements from the surface calculation (top), or the collapsing balloon (center oval) projected onto one image slice. The red arrows are the displacements as calculated from the volumetric deformation algorithm. The right side shows the initial locations of the fiducial markers (colored spheres), as well as the calculated displacements (black lines) projected onto one image slice. The residual errors of the displacement calculation are indicated by the sphere color.
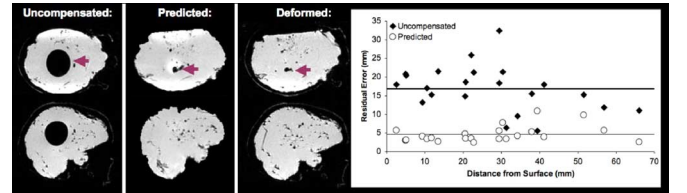

Fig. 8. The left side shows the same (axial, on top, and sagittal, on bottom) slices of the uncompensated, predicted, and deformed (for validation) phantom MR images. The inner balloon (dark arrow) collapses in the deformed image and this is captured by the predicted image. Qualitatively, the predicted image appears similar to the image taken for validation. For quantitative validation, the locations of 22 fiducial markers were located in the uncompensated and deformed images. The distance between these sets of markers represents the uncompensated residual error. The distance between the markers in the predicted and deformed images represents the predicted residual error. The mean errors (16.90 ± 6.17 mm for uncompensated and 4.66 ± 2.26 mm for predicted) are shown with thick and thin lines, respectively, in the graph on the right. In this graph, residual errors at each fiducial marker are plotted versus the distance of the marker to the phantom surface in the uncompensated image.

functional defining the approximation strategy which, in this case, is internal energy. It is defined as $W = \epsilon^T C \epsilon$, where C is a function of spatial position (m), Young's modulus (E), and Poisson's ratio (ν) [34].

In order to produce physiologically correct deformations, (2) was subject to the following constraints:

$$v(s_i^c) = \mathbf{U}_{\text{dense}}(s_i^c) \quad \forall s_i^c \in S^c \tag{3}$$

$$\|(s_k^o + v(s_k^o)) - r_j\| > \delta \quad \forall s_k^o \in S^o, r_j \in R \tag{4}$$

$$v(s_l^f) = 0 \quad \forall s_l^f \in S^f. \tag{5}$$

Equation (3) imposes the known displacements from the surface displacement algorithm ($\mathbf{U}_{\text{dense}}$), by forcing the displacements of the intraoperatively exposed cortical nodes, $v(s_i^c)$, to equal the surface displacement results at those nodes, $\mathbf{U}_{\text{dense}}(s_i^c)$. Equation (4) ensures that all nodes on the brain surface remain some small distance away from the skull. Here, s_k^o are the nodes on the brain surface in the noncraniotomy region S^o, r_j are nodes of the rigid skull surface R, and δ is an arbitrarily small constant. Due to the surface connectivity, (4)

also prevents any nodes from crossing the skull boundary, as this would force other surface nodes to violate this condition. Rather than forcing surface nodes outside the craniotomy region to be fixed, this model constrains the anatomy more realistically. Finally, (5) states that the model deformation of the fixed nodes, s_l^f, within the fixed region, S^f, must be zero.

The constrained minimization defined by (2)–(5) was performed using the finite element analysis software package ABAQUS (ABAQUS, Inc., Providence, RI). The model inputs were the tetrahedral brain mesh, a surface representing the surrounding skull (with craniotomy, see Fig. 10), Poisson's ratio (0.48), and Young's modulus (66.7 kPa) of brain [27]. (The material properties were obtained from the Wayne State University Brain Injury Model, based on 10 years of research from brain impact studies [27].) The cortex and skull surfaces were defined as contact surfaces to enforce the constraints of (4). The output of the finite element analysis was the displacement
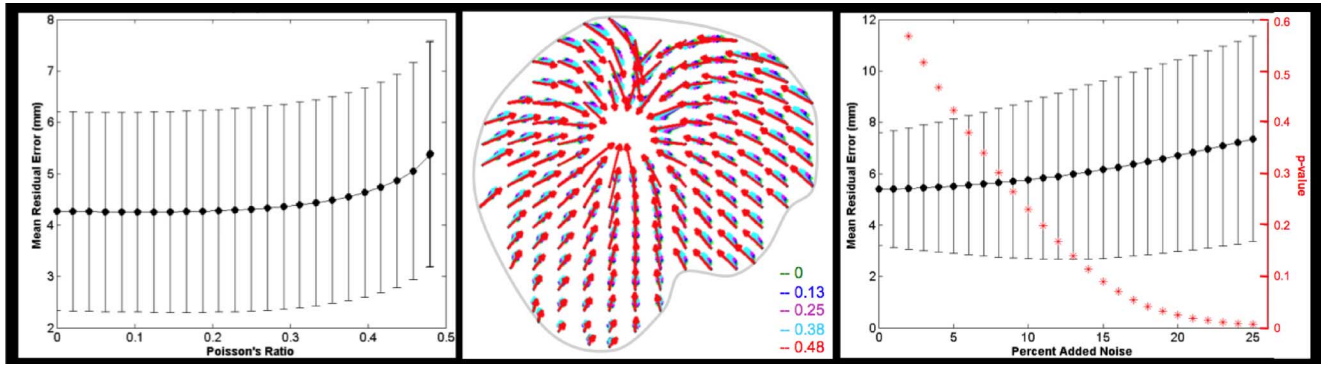
Fig. 9. Left: The mean and standard deviation of the residual volumetric error in half of the brain phantom as a function of Poisson's Ratio. Middle: The deformation in the sagittal plane (perpendicular to surface displacement) of each node for five values of Poisson's Ratio. The red arrows correspond to a Poisson's Ratio of 0.48. Right: The mean and standard deviation of the residual error in half of the brain phantom as a function of noise added to the applied surface displacements are shown in black. Overlaid in red are the p-values of two-tailed paired t-tests performed between the residual errors calculated without added surface displacement noise and the errors calculated using various increments of added noise.
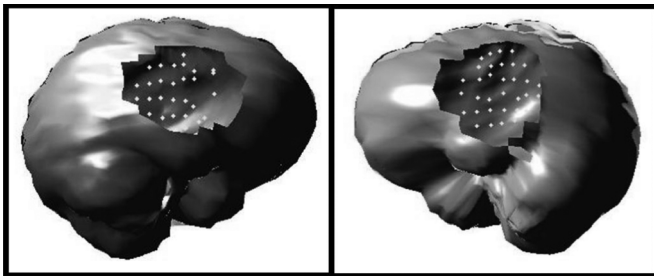

Fig. 10. Deformation constraint surfaces for the bilateral craniotomy. The surfaces depicted in this image act as constraints on the volume deformation. In the craniotomy region, the nodes (bright spheres) are able to move in any direction. However, the non-exposed nodes cannot penetrate the constraining surfaces.

of every node in the brain mesh. Since the goal was to produce a displacement field defined at every point of the original MRI image from which the mesh was obtained, it was necessary to resample the resulting displacements in image space. This was performed using trilinear interpolation.

Mesh elements were uniform with 10 mm side lengths. Mesh generation required less than a minute on a 3 GHz Pentium 4 computer. The volumetric deformation calculations averaged 27 s for this mesh size. The most time consuming step of this process was the trilinear interpolation, which required almost 17 min. Although the deformation calculation using the 10 mm mesh was fast, additional calculations were performed using meshes with shorter side lengths to ensure that the 10 mm mesh did not sacrifice accuracy for speed.

C. Realistic Brain and Skull Phantom

Realistic brain phantoms are commonly used for deformation model validation purposes. The materials used for these physical models are based on the needs of the simulation. Sun *et al.* have shown that translucent agar with visible embedded wires, representing cortical vessels, can be used to simulate deformation in cortical tracking experiments [48]. Audette *et al.* developed a phantom using Polyvinyl Alcohol Cryogel, which can change elasticity based on the number of freeze-thaw cycles used while curing [3]. As an alternative to these materials, several groups have used Dow Corning Sylgard 527 Sil-

icone Dielectric Gel (Dow Corning, Midland, MI) for physical brain modeling in applications including tracking intraoperative brain deformation [38], assessing head trauma sustained from automobile accidents or other brain injuries ([7]–[9], [24], [30], [56], [57]), or development of a training system for transcranial doppler examinations [20]. In previous investigations, this silicone gel has been show to be similar to brain in oscillatory shear and stress relaxation properties, sensitivity to projectile velocity, and ductile response ([23], [56], [57]). These material properties did not vary significantly over large temperature differences or, similar to brain, under large strains [7]. And, in a previous work in which the gel was prepared in a similar manner to this work [56], although the bulk modulus was estimated to be lower than that of brain (1.1 GPa, as opposed to brain's 2.1–2.5 GPa [56]), the gel density (0.98 g/cm^3) was close to that of brain (1.04 g/cm^3). An additional benefit of using this silicone gel is that it cures at room temperature, making it easy to use. It was therefore chosen to create the realistic phantom in this work.

Sylgard 527 Silicone Gel comes in two liquid parts which are mixed to initiate curing. Approximately 550 g of each part were manually combined and poured into a plastic skull mold obtained from the Yale Neurosurgery Department. These molds are created for 3-D visualization of postoperative neurosurgical patients' skulls and are based on patients' MRIs. They are therefore anatomically correct and contain a removable section corresponding to the patients' craniotomies. In this work, the craniotomy was an approximately oval shape centered over the right parietal lobe, with an $\sim$ 10 cm long axis and $\sim$ 8 cm short axis (see Fig. 3, top.) Although a CSF layer was not included in this model, if necessary, CSF could be simulated by placing an additional gel between the silicone gel and skull mold. However, in this work, due to the small size of the CSF layer relative to the deformations induced and the type of deformation tested (i.e., sinking toward the center, rather than bulging outward through the CSF layer and skull opening), the effect of adding a CSF layer would most likely be negligible.

In order to facilitate imaging of the phantom, the surface of the skull mold was coated with a silicone sealant (Silicone II Sealant, GE Sealants and Adhesives, Huntersville, NC) to produce an MR signal. (The uncoated skull mold is visible in

CT.) Immediately after the gel was poured into the skull mold, a latex balloon was placed in its center. The balloon was fully expanded using a calibrated syringe, connected via a three way stopcock to a plastic tube inserted into the balloon. In addition, MR opaque plastic beads were uniformly-distributed throughout the gel. These beads, visible by MRI, were used to validate the volumetric deformation estimation.

After the gel cured (approximately 24 h), another set of radiopaque plastic beads (also visible to the stereo cameras) were attached to the exposed phantom surface in the craniotomy region to simulate cortical features. In addition, the translucent gel surface was painted white (Wite-Out, BIC, Clichy, France) in order to be visible by the stereo cameras, and allow the deformation to be tracked (see Figs. 3–5).

Once cured and painted, deformation could be induced in the phantom by changing the amount of air in the balloon, using the calibrated syringe. With the balloon fully expanded, the phantom surface was rounded and flush against the bottom of the skull mold. Removing air from the balloon causes the surface to sink inward and flatten, as can occur during neurosurgery when gravity or loss of CSF or blood causes the brain surface to sink. Although this design restricts the deformation to a single direction, it allows maximum displacement of the surface inward. With a slightly different design, the phantom may be able to mimic both inward sinking and outward bulging. If the inner balloon is not fully expanded when the phantom cures, the phantom surface can be pushed up through the simulated craniotomy region by expanding the balloon to a larger volume than used during curing.

In the current design, when refilled with air, the phantom surface returns to its position flush against the skull mold. Removal of the same amount of air, as measured by the calibrated syringe, results in repeatable deformation. In this way, the phantom can be used for multiple repeatable experiments.

1) Volumetric Model Validation: As mentioned above, radiopaque plastic beads were placed throughout the volume of the phantom to validate volumetric deformation estimates. These beads appear as dark areas within the phantom, which allow them to be located using a semiautomated strategy. In this strategy, the MR images were automatically searched for fiducial locations using image intensities and known bead volume. Potential fiducial locations were flagged and manually inspected. In order to determine the fiducial marker displacement, the same marker must be located in the initial and deformed images. Matching of markers between images was performed by starting with a fiducial marker located in the initial image and manually searching the space between that location and the balloon center in the deformed image (or the opposite direction when searching for a matching marker in the initial image from a located fiducial marker in the deformed image). The measured displacements were then used to validate the predicted displacements, which were interpolated at the fiducial marker locations using a thin plate spline technique [51] from the displacement of nearby (within three side lengths) brain mesh vertices (deformed using the method explained in Section II-B). The sensitivity of these validation displacement measurements was 1 mm (since the resolution of the MR images acquired for validation was $1 \times 1 \times 1$ mm).

In this work, the initial (uncompensated) error was defined as the distance between the location of a fiducial marker in the initial phantom image and the fiducial's corresponding location in the deflated phantom image. The volumetric algorithm residual error was thus defined as the distance between the interpolated position of the marker and its actual location in the deflated phantom image.

D. Sensitivity Analysis

The finite element model solution is dependent on specified brain material properties, which in this work were based on brain injury models [27]. However, since material stiffness increases with loading rate, brain injury-based parameters may overestimate intraoperative brain stiffness. Therefore, it is essential to determine the sensitivity of the volumetric model to these material parameters. To accomplish this, the model described in (2)–(5) was applied to the brain phantom using Poisson's Ratios ranging from 0 to 0.48. (The maximum value of Poisson's Ratio is 0.5, representing an incompressible material.) Since the homogeneous linear elastic model is driven by displacement conditions only, with no stress on free surfaces, changes in Young's modulus will not affect the model solution; therefore Poisson's ratio, the degree of incompressibility, is the key material property to examine.

In addition to varying Poisson's Ratio, model sensitivity to error in the surface calculation [the $\underline{\mathbf{U}}_{\text{dense}}(s_i^c)$ in (3)] was evaluated. For this analysis, noise was added to the surface displacement estimates, ranging from 1% to 25% of the actual displacement (as measured by the stereo vision technique). The volumetric displacement was then calculated based on the noisy displacements.

To reduce computational complexity, only half of the phantom was used for the sensitivity analysis, along with 17 of the 22 markers that were present within that half of the phantom. (The phantom was divided in half by using all the vertices to one side of a dividing plane down the center of the phantom oriented sagittally.)

E. Experiment Protocol

A similar protocol was followed for both the *in vivo* and phantom deformation experiments.

1) Phantom Protocol: MRIs of the phantom were acquired using the same MR scanner as the *in vivo* cases (Siemens 1.5T Sonata). The initial or "preoperative" MR image was taken while the inner balloon was filled with 130 cc of air. Deformation was then simulated by removing all of the air from the inner balloon, causing it to collapse (see Fig. 3). This deformation was induced while the phantom was inside the MR scanner, using the plastic tube and syringe described in Section II-C, thus preventing the need for an additional registration between MR images of the "preoperative" phantom with the balloon inflated and the "intraoperative" phantom with the balloon deflated (used for validation). After acquisition of the "intraoperative" MR image, the phantom was carefully removed from the scanner. The phantom "preoperative" image was then loaded into a BrainLAB SNS (BrainLAB AG, Munich, Germany). This allowed the full use of BrainLAB's

VectorVision (VV) navigation software, including registration and navigation software [35].

A rigid registration, to correctly orient the SNS to the location of the phantom, was performed using the BrainLAB z-touch tool to sweep an infrared beam across the phantom skull mold, outlining the position of the phantom for the BrainLAB infrared cameras. (Normally, the patient's face is used for this registration.) The BrainLAB system then compares the phantom's physical position with its position in the MR image and performs a rigid registration. Once registered, any point on the phantom can be touched with the BrainLAB pointer tool, and its coordinates returned in MRI space (Fig. 5). These points can be downloaded by connecting to the BrainLAB SNS through the VV Link interface [35] using the Yale BioImage Suite software package [33].

Although the phantom was deformed, the "preoperative" images were loaded into the BrainLAB system. This simulates the way in which preoperative images displayed in the OR do not accurately reflect the intraoperative brain, due to brain shift. To apply the volumetric deformation algorithm, the surface deformation of the phantom was first calculated using the game theoretic algorithm as follows. First, stereo images (images from two camera positions) of the phantom surface were acquired, as in the *in vivo* case (Fig. 3, top). As mentioned in Section II-A2, the initial camera calibration was performed by locating fiducial points on the surface and the stereo images. For this, the positions of five plastic beads on the silicone gel surface (not used in the feature calculation) were used. A standard camera calibration method [49] was then performed using the locations of these beads on the surface, as found by the BrainLAB pointer, and in the stereo images. The result of this calibration is a transformation matrix between physical space and each stereo image, which is used to initialize the calibration parameters [$\mathbf{A}$ in (1)]. The located beads also serve as validation of the surface deformation estimation.

The result of the game theoretic algorithm is the displacement of the phantom surface (and updated calibration parameters). This displacement is then used as an input to the volumetric biomechanical model. Since the phantom contains a balloon that deflates, an additional boundary condition was set on the balloon surface nodes within the phantom mesh to pull the shrinking balloon to its center. This constraint was necessary because the balloon, which is large relative to the phantom brain volume, does not collapse physiologically in the direction of gravity, but rather inward, toward the balloon center. This was the only difference in the volumetric model used for the phantom and *in vivo* cases.

2) In Vivo Protocol: Preoperative MRIs of each patient were acquired on a Siemens 1.5T Sonata system. The acquired MR images were loaded into the BrainLAB SNS, as in the phantom experiment, prior to surgery. Once the patient was moved to the operating room, a rigid registration was performed by sweeping the infrared beam from BrainLAB z-touch tool across the patient's face, allowing the SNS to match its physical location with the location of the patient's face in the MR image. In this work, the volumetric calculation was performed twice on two subjects (Table I).

During surgery, at the time indicated in Table I, stereo images of the patient's exposed cortical surface were acquired. Be-

TABLE I
PATIENT INFORMATION. TWO VOLUMETRIC CALCULATIONS WERE PERFORMED ON EACH PATIENT, USING STEREO IMAGES ACQUIRED AT THE TIME INTO SURGERY INDICATED BY THE LAST COLUMN. (ELECTRODES WERE INSERTED FOR EPILEPSY MONITORING)

Patient #	Age	Sex	Reason for Surgery	Time (min))
1	38	M	electrode insertion (left hemisphere)	230
			electrode insertion (right hemisphere)	230
2	38	M	electrode insertion (right hemisphere)	180
			electrode insertion (right hemisphere)	225

TABLE II
PHANTOM SURFACE DEFORMATION RECOVERY RESULTS IN MILLIMETERS. GAME THEORETIC ALGORITHM CONSTANTS WERE SET TO $\alpha = 4$, $\beta = 0.83$, $\rho = 0.1$, AND $\eta = 25$ [14]. MEAN ALGORITHM ERROR IS LESS THAN 1 MM THOUGH THE PHANTOM SURFACE DEFORMED SIGNIFICANTLY AND CHANGED SHAPE

Error	mean	max	std
Uncompensated	14.71	15.79	0.74
Game Theoretic Algorithm	0.98	1.64	0.58

fore each surface image, a calibration image was acquired. For calibration, a sterile grid of electrodes was placed on the brain surface. Since the electrodes are numbered, they were easily located (and touched with the BrainLAB pointer) by the neurosurgeon and distinguished in the stereo images. A standard camera calibration method [49] was then performed using the locations of these electrodes on the surface and in the stereo images. As with the phantom, these located markers also served as validation of the game theoretic algorithm result.

After the surface deformation was calculated using the game theoretic algorithm outlined above, the deformed surface was used as an input to the volumetric biomechanical model, and the volumetric displacements were calculated.

III. RESULTS

A. Phantom Surface and Volumetric Results

Removing 130 cc of air from the phantom's inner balloon created an average surface deformation of approximately 15 mm (Table II), consistent with the magnitude of cortical shift often observed during neurosurgery ([2], [18], [39], [40]). Fig. 6(A) and (B) shows stereo images of the deflated phantom. Features from the deflated (red), inflated (green), and predicted (by the game theoretic formulation, yellow) phantom surface were projected onto these images (using the projection function P, Section II-A1). Fig. 6(A) shows that the projected features from the inflated surface (green) are not aligned with the imaged features (red), due to the extent of the surface deformation and possible calibration error. However, the game theoretic algorithm was able to predict this surface deformation to within 1 mm on average (Table II), the maximum achievable accuracy due to the resolution of the MRI. The features from the predicted surface, projected with the updated calibration parameters (yellow), are therefore aligned with the imaged features (red).

Fig. 6(C) and (D) shows the image intensities from each camera position backprojected onto the phantom surface. Fig. 6(C) shows the initial (inflated) surface, extracted from the

phantom MRI, with intensities backprojected from the stereo images of the deflated surface. The intensities of the left and right backprojected images are not aligned due to the incorrect surface position and possible calibration errors. In addition, the features on the inflated surface (plastic beads, indicated in green) are not aligned with the backprojected image features (imaged beads). Applying the surface displacement calculated by the game theoretic algorithm yields the surface shown in Fig. 6(D). The backprojected features on this predicted surface (using the updated calibration parameters) are aligned with the deformed feature locations (indicated in yellow), suggesting an accurate surface displacement calculation. As can be seen by the significant difference between the phantom surface in Fig. 6(C) and (D), the induced deformation caused the surface to change position as well as shape, from parabolic to flat.

The calculated surface displacements were then used as the $\mathbf{U}_{\text{dense}}(s_i^c)$ in (3), and the volume deformation was calculated throughout the phantom brain mesh, which consisted of 2210 vertices connected by 9078 elements. The resulting volumetric displacements are shown on the left side of Fig. 7 (for one slice of the brain phantom). As the figure indicates, the largest deformations occur close to the phantom surface and near the collapsing inner balloon.

Twenty-two fiducial markers placed throughout the brain phantom allow determination of the accuracy of the volumetric result in the vicinity of the markers (see Section II-C1). To visualize the spatial distribution of the volumetric algorithm's accuracy, the residual deformation error at each of these marker locations is shown on the right side of Figs. 7 and 8.

As Fig. 8 indicates, although the mean displacement of the markers was quite high (16.90 ± 6.17 mm), the volumetric model predicted most of the deformation. The mean error was reduced to under 5 mm, accounting for 64.4% of the total deformation. In addition, the predicted volumetric image (Fig. 8 left) is similar to the MRI of the deformed phantom, which was performed for validation.

Residual errors in Fig. 8 were plotted versus their distance to the surface. (This distance was manually assessed.) The correlation between the initial distance of the marker from the surface and the residual error was 0.36 and was not significant ($p = 0.10$). For completeness, the correlation between the initial distance of the marker to inner balloon was also calculated. A nonsignificant ($p = 0.49$) negative correlation (-0.16) between these values was found.

Meshes with shorter side lengths did not improve overall model accuracy. Meshes with side length of 5, 7, 8, and 9 mm produced average residual errors of 4.96 ± 2.25, 4.92 ± 2.25, 4.68 ± 2.18, and 4.52 ± 2.01 mm, respectively.

Since solving the LEM for the phantom required both surface (from the game theoretic algorithm) and subsurface (from the collapse of the balloon) boundary conditions, an additional check was performed to determine whether the volumetric deformation could be estimated with less computational expense. For this test, the deformation of the 22 fiducial markers was estimated without the LEM, simply by using a thin plate spline technique [51] to interpolate the marker deformation from the known surface and balloon displacements. Using this technique the estimated error was, on average 91% higher than when the LEM was used (mean error = 8.29 ± 2.92 mm). This drastic increase in residual error is most likely due to the fact that some fiducial markers were not close to nodes with known displacements, making the interpolation in these regions less reliable. This is suggested by the negative correlation (-0.51, $p = 0.01$) between the number of nodes with known displacements within 3 cm of the given fiducial marker and the residual error at that marker.

B. Sensitivity Analysis

The lowest mean error occurred when Poisson's Ratio was set to 0.10 (Fig. 9, left). However, as indicated by the graph, there was little difference in this error over the range of Poisson's Ratios tested. And, there was no significant difference, using a two-tailed paired t-test, between the residual errors at the 17 markers using Poisson's Ratio of 0.10 versus 0.48 ($p = 0.72$, CI = $-0.76 : 1.08$).

Although there were no statistically significant differences in model error, as Poisson's Ratio increases, the defined material becomes less stiff and expands further in response to the same applied compressive displacement. This effect is demonstrated in Fig. 9 (middle) in which the displacement field is calculated in the phantom volume using five different values of Poisson's Ratio. In this figure, the deformation is shown in the plane perpendicular to the applied surface displacement (sagittal plane). Despite the large range of Poisson's Ratios tested, the finite element model successfully converged in all cases tested.

The result of adding increasing values of noise to the surface displacement estimation [the $\mathbf{U}_{\text{dense}}(s_i^c)$ in (3)] is shown on the right side of Fig. 9. The result, as expected, was that residual volumetric error was lowest when there was no added surface displacement noise. As the percent added noise increased, both the mean and standard deviation of the residual volumetric error increased. In red, are the p-values from two-tailed paired t-tests performed between the residual errors found without added noise and the errors calculated with increasing added noise. As the noise increased, the p-values decreased. At 18% noise added, the error differences became statistically significant ($p < 0.05$).

C. In Vivo Data

Volume deformation recovery was then applied to *in vivo* cases as outlined in Section II-E2. The first test case of feasibility was a bilateral craniotomy (Patient 1, Table I). Since the bilateral surgeries were performed simultaneously, the patient had to be oriented so that both hemispheres were accessible (see the skull surfaces used to constrain the deformation, Fig. 10). Because of this, the direction of gravity was parallel to the plane of the dural openings rather than perpendicular to them, as is normally the case.

The mean (and maximum) cortical surface displacement was 6.37 mm (12.09 mm) and 4.13 mm (7.78 mm) for the left and right craniotomy respectively. However, using the game theoretic surface tracking algorithm, this displacement error was reduced to 1.26 mm (3.02 mm) and 0.88 mm (1.37 mm), respectively (data presented previously [14]). The cortical displacement, as determined by the using game theoretic algorithm, was
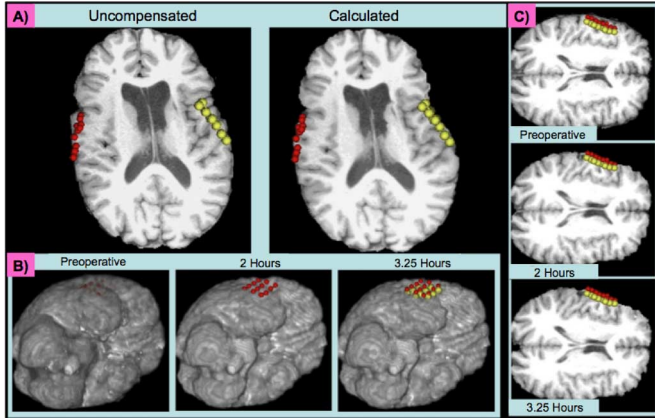
Fig. 11. (A) An axial slice of the preoperative MRI (left) which has been deformed using the linear elastic model (right). The red and yellow spheres indicate the surface points acquired during surgery. (B) Volume renderings of the preoperative (left) and predicted (middle and right) MR images. The red spheres were acquired by the neurosurgeon 2 h into surgery and the yellow spheres were acquired 75 min later. (C) One axial slice of the preoperative (top) and predicted (middle and bottom) MR images from (B). As the surface sinks toward the midline over time, the deformation is propagated through the hemisphere and the ventricle begins to collapse. The same red and yellow spheres from (B) are plotted here relative to the single MR image slice.

extended to the volume using the linear elastic model developed in this work. The mesh created for the volumetric calculation contained 2469 vertices, connected by 10 645 elements, with 736 surface nodes. As mentioned above, orientation of the patient's head in the OR is not an input to the LEM; however, as the results in Fig. 11(A) indicate, the deformation estimate did not require this information.

Volumetric model deformation calculations were also performed on two sets of data acquired at two separate times during surgery (Patient 2, Table I). In this way, the temporal course of deformation can be examined. The mean (and maximum) cortical surface displacement was 4.48 mm (5.83 mm) and 6.59 mm (12.32 mm) at 2 and 3.25 h into surgery, respectively. Using the game theoretic surface tracking algorithm, this displacement error was reduced to 0.60 mm (1.52 mm) and 0.39 mm (0.63 mm), respectively (data presented previously [14]). As in the bilateral craniotomy cases, the cortical displacement, as found using the game theoretic formulation, was extended to the volume using the LEM. The brain mesh for this subject consisted of 1503 vertices, connected by 5907 elements, with 568 surface nodes.

Fig. 11(B) shows the surface deformation over time relative to the fiducial electrode locations on the brain surface acquired 2 h into surgery (red) and 3.25 h into surgery (yellow). From this view, a gradual shift downward can be seen on the surface. Fig. 11(C) shows the same deformation in one slice of the MR image. The results at 2 and 3.25 h, though calculated independently, are consistent with each other in that they portray a gradually increasing deformation.

IV. CONCLUSION AND FUTURE WORK

A. Summary

Several important contributions are described in this work. A linear elastic model to quantify volumetric brain deformation

was developed that only requires the cortical displacement (as found by any cortical surface tracking technique) and the material properties of brain as inputs. A silicone phantom was designed and built. This realistic phantom allowed: 1) evaluation of the sensitivity to model inputs (Poisson's Ratio and noise in the cortical surface estimation), 2) testing, for the first time, of the surface tracking and volumetric model applied together and, as such, 3) estimates of both surface tracking and volumetric LEM residual error. In addition to the model development and testing in the phantom, the LEM in this work was applied to *in vivo* cases in the context of neocortical epilepsy surgery. The differences in these cases allowed further confirmation the feasibility of applying this deformation compensation technique *in vivo*. Each of these contributions are further described below.

1) Linear Elastic Model: The LEM developed in this work extends cortical surface deformation results to the brain volume. This model requires minimal inputs, is easy to implement (can be applied to any brain mesh, using any surface deformation estimate), and is not computational expensive (the whole brain deformation can be calculated in under a minute). Despite this, the linear elastic model was able to account for most of the large deformation induced in a brain phantom experiment. In this validation experiment, without volumetric compensation, the localization error at the 22 markers was almost 17 mm, on average. That magnitude of deformation could result in localization difficulties during surgery. Using the volumetric compensation, however, the mean error was decreased to under 5 mm. Although most neurosurgical applications will require greater sensitivity than this, the significant reduction in error from the uncompensated state provides an important step forward for neurosurgical navigation and suggests the benefits of this type of solution. In addition, the comparison of the LEM model results to those obtained using only a thin plate spline show the advantages of using a biomechanical model defined throughout the brain volume. Qualitative assessment of the deformation estimated in the *in vivo* cases also suggests the effectiveness of this developed LEM.

2) Brain Phantom: Due to its shape and material properties, the realistic phantom developed in this work allowed evaluation of both the surface tracking and volumtric models. Despite the large deformation induced, which caused drastic changes in the shape of the phantom surface, both the deformed surface position and shape were predicted by the game theoretic algorithm. This was an important test of the game theoretic algorithm's robustness because cortical shift is often not constant over the exposed surface in *in vivo* cases. The phantom was able to simulate this well, as indicated in Fig. 8 (right) by the range of induced deformations. And, although this game-theoretic surface tracking algorithm was previously successfully applied to several *in vivo* cases [14], the validation performed in this work provides greater confidence in the ability of this algorithm to produce accurate results in cases of extreme deformation.

Estimation of LEM error using the phantom was also an important step in model development, as quantitative volumetric *in vivo* validation is often not feasible. The phantom allowed both quantification of model error and visualization of error distribution. The latter analysis is informative since intraoperative information is usually available only at the brain surface, and

therefore localization accuracy may decrease with depth. In this work, however, there appeared to be little correlation between residual model error and depth, as indicated in Fig. 7 (right) and Fig. 8 (right). This may potentially be due to the additional constraint on the balloon deformation within the phantom, however, the correlation between residual error and distance to the inner balloon was also small.

3) Sensitivity Analysis: The brain phantom allowed analysis of the sensitivity of the predicted model displacements to Poisson's Ratio and the applied surface displacements. Although greater values of Poisson's Ratio appeared to increase the material displacement in the plane perpendicular to the brain deformation (Fig. 9, middle), this did not result in significant differences in residual model error. This is most likely because the majority of the deformation (which occurred in the direction of gravity) was imposed by the surface displacement, and therefore the resulting volumetric displacement was not greatly affected by the chosen material properties. However, although the differences in model error were not significant, the fact that the errors increased as Poisson's Ratio increased may signal that the silicone gel used in this experiment was stiffer than expected.

As opposed to changes in Poisson's Ratio, Fig. 9 (right) indicates that errors in the surface displacement estimation can significantly affect LEM displacement results. After a certain threshold of noise (18%), the surface displacement errors significantly increased. This underscores the need for accurate surface detection. Although the game theoretic algorithm substantially reduced the uncompensated surface localization error (Table II), any residual surface displacement error was propagated throughout the volume, contributing to the residual volumetric error.

B. Future Work

In order to use this technique in a range of surgeries, the following must be addressed:

1) Quantitative In Vivo Volumetric Validation: Phantom validation experiments are extremely useful because they provide control over the type and extent of deformation induced, and allow algorithm validation in extreme conditions. However, it is also important to validate the algorithm quantitatively *in vivo*. Although the silicone phantom deformed in a manner consistent with brain, the large inflatable balloon induced a nonphysiological component to the deformation. To account for the balloon collapse, an extra constraint (pulling balloon surface to its center) had to be added to the model. This term provided additional information within the phantom volume that may not be available *in vivo* and therefore, may have provided additional model accuracy in regions close to the balloon. However, for many *in vivo* applications (except for large resections, see below), the largest deformation would occur at the brain surface where it could be monitored by the stereo cameras, so removal of this term may not affect model accuracy. Although the qualitative *in vivo* results in this work suggest this, further testing is necessary for verification. This could be accomplished, for example, by using an intraoperative volumetric imaging modality to locate various deep brain structures and comparing their predicted positions to their imaged locations.

2) Properties: One of the difficulties in estimating brain biomechanical properties is the complexity of the deformation response. In addition, even brain model boundary conditions, such as inclusion of rigid brain sections, brain stem and skull base can affect the analysis outcome [50]. However, it is precisely because of this complexity that simplifying assumptions are required to model the system. In this work, the brain is treated as a homogenous material. This may not be appropriate for all *in vivo* cases. For example, in the work of Hu *et al.* [22], a finite element model consisting of different material properties for grey matter, white matter, brainstem, and cerebellum was used, in addition to including effects of CSF drainage. This more complex model may yield finer results in certain areas of the brain; however, the issue of how to set these parameters remains. Since the *in vivo* material properties of human brain are usually not available, the selection of these parameters will be subjective [22]. Also, the additional parameter added for model refinement in that work, the amount of CSF drainage, had to be assumed and therefore led to an over estimation of brain deformation. This suggests that a more detailed model may only improve accuracy when those detailed parameters are known.

In addition, evidence suggests that material properties may change with aging, or due to disease [41]. This complicates the modeling even further. For example, there is no literature on the mechanical properties of brain tumors [54]. Therefore, to create a universally-applicable brain model, it may be necessary to estimate patient-specific brain material properties. This could be accomplished, for example, using magnetic resonance elastography [41]. The necessary level of detail for brain material properties remains an open problem.

3) Mesh Size: In this work, a uniform tetrahedral mesh with 10 mm elements was used. This mesh size was appropriate for the phantom, as indicated by the consistent results across mesh side lengths from 5–10 mm. This is most likely because the phantom did not contain fine structures. It is possible, however, that *in vivo* surgical applications may require meshes of different sizes. To obtain finer resolution around structures of interest, smaller mesh elements could be used in these regions, which may result in longer required computation time. This can be avoided by using larger mesh elements in regions farther away from the surgical target. By using a nonuniform mesh in this way, fine resolution can be obtained in critical areas, without sacrificing computational time. Development of these types of meshes will depend on the type of surgery and the visualization needs.

4) Workflow: It is helpful to outline a potential workflow for applying this type of system for deformation recovery *in vivo*. As indicated in Fig. 1, before surgery, a preoperative MRI is acquired and the brain and skull mesh are created (∼1 min). During surgery, the neurosurgeon can use commercial surgical guidance (which does not account for soft tissue deformation). However, as soon as there is a noted deviation between the intraoperative brain and the preoperative images, the stereo-guided volumetric algorithm can be run. This deviation can be discovered, for example, by using the pointer tool to touch a point on the cortical surface. When the pointer tool is displayed on the surgical navigation system, relative to the preoperative brain, it may appear that the pointer is touching a region under, or above, the brain surface (because the brain surface has shifted). At that

time, or any time the surgical path is near a functionally eloquent region, the surgeon can choose to update the preoperative images.

The update would proceed as follows. A digital camera (ORs normally have a ceiling mounted camera to document surgeries) would take a series of four images: 1) a calibration image (image of an object of known dimensions), 2) an image of the brain surface (without changing camera position from image 1), 3) a calibration image in a new camera position, and 4) an image of the brain surface (without changing camera position from image 3). This entire procedure can be performed in under five minutes. After that, all acquisitions are complete, and the surgery can proceed while feature and fiducial localization is performed and the updated images are computed. This computation consists of updating the initial calibration parameters (calculated from the calibration images) and determination of the cortical surface movement using the game theoretic algorithm. The deformed surface is then used as a boundary condition for the biomechanical model, the volumetric results calculated, and the interpolated image created. This type of update can be repeated as often as needed, or in conjunction with introperative volumetric imaging (see below).

This description of the workflow assumes that the image update can be performed in real time (i.e., on the order of minutes). Currently, the computations described above require ~ 30 min for completion. However, this system was designed for development purposes only. The computation currently does not take advantage of parallel computing or more powerful computational processors. When the process is updated in this way, the computation will be able to provide updated images for surgical guidance in minutes.

5) Use With Intraoperative Volumetric Imaging: The most challenging cases for volumetric deformation recovery are large resections, i.e., temporal lobectomies or tumor resections. In these cases, a biomechanical model based on the preoperative brain would no longer be valid and some type of volumetric intraoperative imaging would be necessary. However, during these surgeries, the LEM-based deformation technique can be used to update the preoperative images and guide the surgery until the resection, or until a threshold deformation magnitude is reached. At that point, an image from a volumetric imaging modality could be acquired to quantify the amount of tissue removed, and an updated mesh of the brain could be created based on that volumetric image. The LEM-based deformation estimation can then resume with the updated mesh. The current study lays the foundation for this type of process. Similar to the inner balloon of a phantom, once the size and location of the resected region is quantified, the removal or collapsing of the associated mesh nodes can be reflected in the volumetric model, for continued surgical guidance. This combined volumetric imaging/model estimation method would decrease the number of intraoperative volume scans required and therefore greatly reduce image acquisition (and total surgical) time. Even if a biomechanical model-based technique could not be used postresection (for example, if the solution accuracy were compromised by the magnitude of the resection), using the LEM-based technique from dural opening until the point of resection would still provide the considerable advantages of improved guidance and reduced acquisition time until resection.

C. Conclusion

SNS have already proven to be a beneficial addition to neurosurgery. The aid that SNS provide in localizing pathologic tissue is invaluable. However, due to brain deformation, their use is limited to guidance before the brain has shifted or providing only limited information after the shift. In this work and our previous work [14], a comprehensive 3-D brain deformation compensation model has been developed which can track this cortical shift and use the estimated cortical displacement to determine volumetric deformation. Incorporating this system into current SNS guidance systems would result in more accurate surgical guidance, leading to better detection of pathologic tissue and decreased surgical complications.

REFERENCES

[1] N. Archip, A. Fedorov, B. Lloyd, N. Chrisochoides, A. Golby, P. M. Black, and S. K. Warfield, "Integration of patient specific modeling and advanced image processing techniques for image-guided neurosurgery," in *Med. Ima. 2006: Visualizat., Image-Guided Procedures, Display, Proc. SPIE*, San Diego, CA, Feb. 12–14, 2006, vol. 6141, pp. 422–429.

[2] M. A. Audette, K. Siddiqi, F. P. Ferrie, and T. M. Peters, "An integrated range-sensing, segmentation and registration framework for the characterization of intra-surgical brain deformations in image-guided surgery," *Comput. Vis. Image Understand.*, vol. 89, no. 2-3, pp. 226–251, Feb.-Mar. 2003.

[3] M. A. Audette, K. Siddiqi, and T. M. Peters, "Level-set surface segmentation and fast cortical range image tracking for computing intra-surgical deformations," in *Medical Image Computing and Computer-Assisted Intervention (MICCAI)*, Cambridge, U.K., Sep. 19–22, 1999, vol. 1679, pp. 788–797.

[4] L. M. Bates, S. J. Goerss, and R. A. Robb, "A method for quantitative validation of image based correction for intraoperative brain shift," in *Med. Imag. 2000: Image Display Visulaizat., Proc. SPIE*, San Diego, CA, Feb. 13–15, 2000, vol. 3976, pp. 58–69.

[5] T. Blumenthal, A. Hartov, K. Lunn, F. E. Kennedy, D. W. Roberts, and K. D. Paulsen, "Quantifying brain shift during neurosurgery using spatially tracked ultrasound," in *Med. Imag. 2005: Visualizat., Image-Guided Procedures, Display, Proc. SPIE*, San Diego, CA, Feb. 13–15, 2005, vol. 5744, pp. 388–399.

[6] A. F. Bower, "Constitutive models – Relations between stress and strain," in *Applied Mechanics of Solids*. Boca Raton, FL: CRC Press, 2009, pp. 69–87.

[7] D. R. S. Bradshaw, J. Ivarsson, C. L. Morfey, and D. C. Viano, "Simulation of acute subdural hematoma and diffuse axonal injury in coronal head impact," *J. Biomechan. Eng.*, vol. 34, no. 1, pp. 85–94, Jan. 2001.

[8] D. W. A. Brands, P. H. M. Bovendeerd, G. W. M. Peters, J. S. H. M. Wismans, M. H. J. W. Paas, and J. L. M. J. van Bree, L. L. Ricci, Ed., "Comparison of the dynamic behaviour of brain tissue and two model materials," in *Proc. 43rd Stapp Car Crash Conf.*, 1999, pp. 313–320.

[9] D. W. A. Brands, P. H. M. Bovendeerd, and J. S. H. M. Wismans, "On the potential importance of non-linear viscoelastic material modelling for numerical prediction of brain tissue response: Test and application," *Stapp Car Crash J.*, vol. 46, pp. 103–21, Nov. 2002.

[10] A. Cao, P. Dumpuri, and M. I. Miga, "Tracking cortical surface deformations based on vessel structure using a laser range scanner," in *Int. Symp. Biomed. Imag. (ISBI)*, Washington, DC, Apr. 6–9, 2006, pp. 522–525.

[11] A. Cao, R. C. Thompson, P. Dumpuri, B. M. Dawant, R. L. Galloway, S. Ding, and M. I. Miga, "Laser range scanning for image-guided neurosurgery: Investigation of image-to-physical space registrations," *Med. Phys.*, vol. 35, no. 4, pp. 1593–1605, Mar. 2008.

[12] I. Chen, A. M. Coffey, S. Ding, P. Dumpuri, B. M. Dawant, R. C. Thompson, and M. I. Miga, "Intraoperative brain shift compensation: Accounting for dural septa," *IEEE Trans. Biomed. Eng.*, vol. 58, no. 3, pp. 499–508, Mar. 2011.

[13] O. Clatz, H. Delingette, I. F. Talos, A. J. Golby, R. Kikinis, F. A. Jolesz, N. Ayache, and S. K. Warfield, "Robust nonrigid registration to capture brain shift from intraoperative MRI," *IEEE Trans. Med. Imag.*, vol. 24, no. 11, pp. 1417–1427, Nov. 2005.

[14] C. DeLorenzo, X. Papademetris, L. H. Staib, K. P. Vives, D. D. Spencer, and J. S. Duncan, "Image-guided intraoperative cortical deformation recovery using game theory: Application to neocortical epilepsy surgery," *IEEE Trans. Med. Imag.*, vol. 29, no. 2, pp. 322–338, Feb. 2010.

[15] S. Ding, M. I. Miga, J. H. Noble, A. Cao, P. Dumpuri, R. C. Thompson, and B. M. Dawant, "Semiautomatic registration of pre- and postbrain tumor resection laser range data: Method and validation," *IEEE Trans. Biomed. Eng.*, vol. 56, no. 3, pp. 770–779, Mar. 2009.

[16] S. Ding, M. I. Miga, T. S. Pheiffer, A. L. Simpson, R. C. Thompson, and B. M. Dawant, "Tracking of vessels in intra-operative microscope video sequences for cortical displacement estimation," *IEEE Trans. Biomed. Eng.*, vol. 58, no. 7, pp. 1985–1993, Jul. 2011.

[17] P. Dumpuri, R. C. Thompson, B. M. Dawant, A. Cao, and M. I. Miga, "An atlas-based method to compensate for brain shift: Preliminary results," *Med. Image Anal.*, vol. 11, no. 2, pp. 128–145, Apr. 2007.

[18] M. Ferrant, A. Nabavi, B. Macq, P. M. Black, F. A. Jolesz, R. Kikinis, and S. K. Warfield, "Serial registration of intraoperative MR images of the brain," *Med. Image Anal.*, vol. 6, no. 4, pp. 337–359, Dec. 2002.

[19] D. G. Gobbi, R. M. Comeau, and T. M. Peters, "Ultrasound/MRI overlay with image warping for neurosurgery," in *Med. Image Computing Computer-Assisted Intervent. (MICCAI)*, Pittsburgh, PA, Oct. 11–14, 2000, vol. 1935, pp. 106–114.

[20] R. Hart, P. D. Hart, and S. Bunt, "A novel technique for simulating transcranial doppler examinations in vitro," in *Medical Image Computing and Computer-Assisted Intervention (MICCAI)*, Cambridge, U.K., Sep. 19–22, 1999, vol. 1679, pp. 1226–1233.

[21] P. Hastreiter, C. Rezk-Salama, G. Soza, M. Bauer, G. Greiner, R. Fahlbusch, O. Ganslandt, and C. Nimsky, "Strategies for brain shift evaluation," *Med. Image Anal.*, vol. 8, no. 4, pp. 447–464, Dec. 2004.

[22] J. Hu, X. Jin, J. B. Lee, L. Zhang, V. Chaudhary, M. Guthikonda, K. H. Yang, and A. I. King, "Intraoperative brain shift prediction using a 3-D inhomogeneous patient-specific finite element model," *J. Neurosurg.*, vol. 106, no. 1, pp. 164–169, Jan. 2007.

[23] J. Ivarsson, D. C. Viano, and P. Lövsund, "Influence of the lateral ventricles and irregular skull base on brain kinematics due to sagittal plane head rotation," *J. Biomechan. Eng.*, vol. 124, no. 4, pp. 181–189, Aug. 2002.

[24] J. Ivarsson, D. C. Viano, P. Lövsund, and B. Aldman, "Strain relief from the cerebral ventricles during head impact: Experimental studies on natural protection of the brain," *J. Biomechan.*, vol. 33, no. 2, pp. 422–431, Feb. 2000.

[25] S. Ji, A. Hartov, D. Roberts, and K. Paulsen, "Data assimilation using a gradient descent method for estimation of intraoperative brain deformation," *Med. Image Anal.*, vol. 13, pp. 744–756, 2009.

[26] C. A. Kemper, I. F. Talos, A. Golby, P. M. Black, R. Kikinis, W. E. L. Grimson, and S. K. Warfield, "An anisotropic material model for image guided neurosurgery," in *Medical Image Computing Computer-Assisted Intervent. (MICCAI)*, Saint-Malo, France, Sep. 26–29, 2004, vol. 3217, pp. 267–275.

[27] A. I. King, K. H. Yang, and T. Khalil, WSU Brain Injury Model [Online]. Available: http://ttb.eng.wayne.edu/brain/

[28] M. M. J. Letteboer, P. W. A. Willems, M. A. Viergever, and W. J. Niessen, "Brain shift estimation in image-guided neurosurgery using 3-D ultrasound," *IEEE Trans. Biomed. Eng.*, vol. 52, no. 2, pp. 268–276, Feb. 2005.

[29] K. E. Lunn, K. D. Paulsen, D. R. Lynch, D. W. Roberts, F. E. Kennedy, and A. Hartov, "Assimilating intraoperative data with brain shift modeling using the adjoint equations," *Med. Image Anal.*, vol. 9, no. 3, pp. 281–293, Jun. ,2005.

[30] S. S. Margulies, L. E. Thibault, and T. A. Gennarelli, "Physical model simulations of brain injury in the primate," *J. Biomechan.*, vol. 23, no. 8, pp. 823–836, 1990.

[31] S. Nakajima, H. Atsumi, R. Kikinis, T. M. Moriarty, D. C. Metcalf, F. A. Jolesz, and P. M. Black, "Use of cortical surface vessel registration for image-guided neurosurgery," *Neurosurgery*, vol. 40, pp. 1201–1210, Jun. 1997.

[32] C. Nimsky, O. Ganslandt, B. v. Keller, and R. Fahlbusch, "Intraoperative high-field MRI: Anatomical and functional imaging," *Acta Neurochir*, pp. 87–95, 2006.

[33] X. Papademetris, M. Jackowski, N. Rajeevan, R. T. Constable, and L. H. Staib, BioImage Suite: An integrated medical image analysis suite Yale School of Med., Section Bioimag. Sci., Dept. Diagnostic Radiol. [Online]. Available: http://www.bioimagesuite.org

[34] X. Papademetris, O. Škrinjar, and J. S. Duncan, "Recovering displacements and deformations from 3-D medical images using biomechanical models," in *Computational Models for the Human Body: Special*. Amsterdam, The Netherlands: Elsevier B.V., 2004, vol. 12, Handbook of Numerical Analysis, pp. 551–590.

[35] X. Papademetris, K. P. Vives, M. DiStasio, L. H. Staib, M. Neff, S. Flossman, N. Frielinghaus, H. Zaveri, E. J. Novotny, H. Blumenfeld, R. T. Constable, H. P. Hetherington, R. Duckrow, S. S. Spencer, D. D. Spencer, and J. S. Duncan, "Development of a research interface for image guided intervention: Initial application to epilepsy neurosurgery," in *Int. Symp. Biomed. Imag. (ISBI)*, Washington, DC, USA, Apr. 6–8, 2006, pp. 490–493.

[36] P. Paul, X. Morandi, and P. Jannin, "A surface registration method for quantication of intraoperative brain deformations in image-guided neurosurgery," *IEEE Trans. Inf. Technol. Biomed.*, vol. 13, no. 6, pp. 976–983, Nov. 2009.

[37] K. D. Paulsen, M. I. Miga, F. E. Kennedy, P. J. Hoopes, A. Hartov, and D. W. Roberts, "A computational model for tracking subsurface tissue deformation during stereotactic neurosurgery," *IEEE Trans. Biomed. Eng.*, vol. 46, no. 2, pp. 213–225, Feb. 1999.

[38] A. Puzrin, O. Škrinjar, C. Ozan, S. Kim, and S. Mukundan, "Image guided constitutive modeling of the silicone brain phantom," in *Med. Imag. 2005: Visualizat., Image-Guided Procedures, Display, Proc. SPIE*, San Diego, CA, Feb. 13–15, 2005, vol. 5744, pp. 157–164.

[39] I. Reinertsen, M. Descoteaux, S. Drouin, K. Siddiqi, and D. L. Collins, "Vessel driven correction of brain shift," in *Med. Image Computing Computer-Assisted Intervent. (MICCAI)*, Saint-Malo, France, Sep. 26–29, 2004, vol. 3217, pp. 208–216.

[40] D. W. Roberts, A. Hartov, F. E. Kennedy, M. I. Miga, and K. D. Paulsen, "Intraoperative brain shift and deformation: A quantitative analysis of cortical displacement in 28 cases," *Neurosurgery*, vol. 43, no. 4, pp. 749–758, Oct. 1998.

[41] I. Sack, B. Beierbach, J. Wuerfel, D. Klatt, U. Hamhaber, S. Papazoglou, P. Martus, and J. Braun, "The impact of aging and gender on brain viscoelasticity," *Neuroimage*, vol. 46, no. 3, pp. 652–657, Mar. 2009.

[42] T. K. Sinha, B. D. Dawant, V. Duay, D. M. Cash, R. J. Weil, R. C. Thompson, K. D. Weaver, and M. I. Miga, "A method to track cortical surface deformations using a laser range scanner," *IEEE Trans. Med. Imag.*, vol. 24, no. 6, pp. 767–781, Jun. 2005.

[43] T. K. Sinha, M. I. Miga, D. M. Cash, and R. J. Weil, "Intraoperative cortical surface characterization using laser range scanning: Preliminary results," *Neurosurgery*, vol. 59, pp. ONS368–ONS377, Oct. 2006.

[44] O. Škrinjar, A. Nabavi, and J. S. Duncan, "A stereo-guided biomechanical model for volumetric deformation analysis," in *Math. Methods Biomed. Image Anal. (MMBIA)*, Kauai, HI, Dec. 9–10, 2001, pp. 95–102.

[45] O. Škrinjar, A. Nabavi, and J. S. Duncan, "Model-driven brain shift compensation," *Med. Image Anal.*, vol. 6, no. 4, pp. 361–373, Dec. 2002.

[46] G. Soza, R. Grosso, C. Nimsky, G. Greiner, and P. Hastreiter, "Estimating mechanical brain tissue properties with simulation and registration," in *Med. Image Comput. Computer-Assisted Intervent. (MICCAI)*, Saint-Malo, France, Sep. 26–29, 2004, vol. 3217, pp. 276–283.

[47] H. Sun, K. E. Lunn, H. Farid, Z. Wu, D. W. Roberts, A. Hartov, and K. D. Paulsen, "Stereopsis-guided brain shift compensation," *IEEE Trans. Med. Imag.*, vol. 24, no. 8, pp. 1039–1052, Aug. 2005.

[48] H. Sun, D. W. Roberts, A. Hartov, K. Rick, and K. D. Paulsen, "Using cortical vessels for patient registration during image-guided neurosurgery – A phantom study," in *Med. Imag. 2003: Visualizat., Image-Guided Procedures, Display, Proc. SPIE*, San Diego, CA, Feb. 16–18, 2003, vol. 5029, pp. 183–191.

[49] E. Trucco and A. Verri, *Introductory Techniques for 3-D Computer Vision*. Upper Saddle River, NJ: Prentice-Hall, 1998.

[50] K. Voo, S. Kumaresan, F. A. Pintar, N. Yoganandan, and A. Sances Jr., "Finite-element models of the human head," *Med. Biol. Eng. Comput.*, vol. 34, no. 5, pp. 375–381, Sep. 1996.

[51] G. Wahba, *Spline Models for Observational Data*. Montpelier, VT: Capital City Press, 1992.

[52] S. K. Warfield, F. Talos, A. Tei, A. Bharatha, A. Nabavi, M. Ferrant, P. M. Black, F. A. Jolesz, and R. Kikinis, "Real-time registration of volumetric brain MRI by biomechanical simulation of deformation during image guided neurosurgery," *Comput. Visualizat. Sci.*, vol. 5, no. 1, pp. 3–11, Jul. 2002.

[53] A. Wittek, R. Kikinis, S. K. Warfield, and K. Miller, "Brain shift computation using a fully nonlinear biomechanical model," in *Med. Image Comput. Computer-Assisted Intervent. (MICCAI)*, Palm Springs, CA, Oct. 26–29, 2005, vol. 3750, pp. 583–590.

[54] A. Wittek, K. Miller, R. Kikinis, and S. K. Warfield, "Patient-specific model of brain deformation: Application to medical image registration," *J. Biomechan.*, vol. 40, no. 4, pp. 919–929, May 2007.

[55] C. Zhang, M. Wang, and Z. Song, "A brain-deformation framework based on a linear elastic model and evaluation using clinical data," *IEEE Trans. Biomed. Eng.*, vol. 58, no. 1, pp. 191–199, Jan. 2011.

[56] J. Zhang, F. A. Pintar, N. Yoganandan, T. A. Gennarelli, and S. F. Son, "Experimental study of blast-induced traumatic brain injury using a physical head model," *Stapp Car Crash J.*, vol. 53, pp. 215–227, Nov. 2009.

[57] J. Zhang, N. Yoganandan, F. A. Pintar, Y. Guan, and T. A. Gennarelli, "Experimental model for civilian ballistic brain injury biomechanics quantication," *J. Biomechan.*, vol. 40, no. 10, p. 23412346, 2007.